Journal of Geophysical Research: Oceans

RESEARCH ARTICLE
10.1029/2018JC013999

First Direct Estimates of Volume and Water Mass Transports Across the Reykjanes Ridge

Tillys Petit[1], **Herlé Mercier**[2], **and Virginie Thierry**[1]

[1]Ifremer, University of Brest, CNRS, IRD, Laboratoire d'Océanographie Physique et Spatiale (LOPS), IUEM, Brest, France, [2]CNRS, University of Brest, IRD, Ifremer, Laboratoire d'Océanographie Physique et Spatiale (LOPS), IUEM, Brest, France

Key Points:
- The subpolar gyre (SPG) intensity was estimated at 21.9 ± 2.5 Sv in summer 2015
- The westward limb of the SPG was intensified at the Bight Fracture Zone (57°N) and at 59–62°N
- Horizontal circulation, mixing, and bathymetry shaped the water mass distribution over the Reykjanes Ridge

Correspondence to:
T. Petit,
tillys.petit@ifremer.fr

Citation:
Petit, T., Mercier, H., & Thierry, V. (2018). First direct estimates of volume and water mass transports across the Reykjanes Ridge. *Journal of Geophysical Research: Oceans*, *123*, 6703–6719. https://doi.org/10.1029/2018JC013999

Received 21 MAR 2018
Accepted 22 AUG 2018
Accepted article online 29 AUG 2018
Published online 19 SEP 2018

Abstract The Reykjanes Ridge is a major topographic feature located south of Iceland in the North Atlantic Ocean that strongly influences the subpolar gyre circulation. Based on velocity and hydrographic measurements carried out along the crest of the Reykjanes Ridge from the Icelandic continental shelf to 50°N during the RREX cruise in June–July 2015, we derived the first direct estimates of volume and water mass transports over the Reykjanes Ridge. North of 53.15°N, circulation was mainly westward; south of this latitude it was mainly eastward. The westward transport was estimated at 21.9 ± 2.5 Sv (Sv = 10^6 m^3 s^{-1}) and represents the subpolar gyre intensity. The westward flows followed two main pathways at 57°N near the Bight Fracture Zone and at 59–62°N. We argue that those pathways were connected to the northern branch of the North Atlantic Current and to the Sub-Arctic Front, respectively, which were both intersected by the southern part of the section. In addition to this horizontal circulation, mixing and bathymetry shaped the water mass distribution. Water mass transformations in the Iceland Basin lead to the formation of weakly stratified Subpolar Mode Water. We explain why Subpolar Mode Water, the main water mass contributing to the westward flow, was denser at 57°N than at 59–62°N. At higher densities, both Intermediate Water and Icelandic Slope Water contributed more to the westward transport across the Reykjanes Ridge than the sum of Labrador Sea Water and Iceland-Scotland Overflow Water.

Plain Language Summary The Reykjanes Ridge, the northern section of the Mid-Atlantic Ridge, strongly influences the cyclonic circulation of the North Atlantic subpolar gyre, a major component of the climate system. Up to now, no dedicated data set was available to describe the circulation across this ridge. To fill this gap, surface-to-bottom measurements of flow velocity and water mass properties were carried out along the crest of the ridge, from Iceland to 50°N, in 2015. North of 53.15°N, the flow was mainly westward. It defines the westward branch of the subpolar gyre, and our study provides the first direct estimate of its intensity. The westward flow followed two main pathways related to specific bathymetry features: at the Bight Fracture Zone (57°N), which is a deep opening in the ridge, and at 59–62°N where the bathymetry rapidly deepens southward. The horizontal circulation of the Iceland Basin connects these pathways to the North Atlantic Current flowing eastward south of 53.15°N. Knowledge of the westward cross-ridge flows is a prerequisite for understanding the northward evolution of the Irminger Current, a major conduit for the subtropical waters toward the deep convection regions in the Irminger and Labrador Seas.

1. Introduction

The Reykjanes Ridge, which is located at the northern part of the Mid-Atlantic Ridge (MAR), is a major topographic feature of the northern North Atlantic. Located between the Iceland Basin, to the east, and the Irminger Sea, to the west, the Reykjanes Ridge extends along a northeast/southwest line from Iceland to 55°N, south of the Bight Fracture Zone (BFZ), and then along a more meridional line to the Charlie Gibbs Fracture Zone (CGFZ) at 52.5°N (Figure 1). At the CGFZ, the MAR shifts eastward. The summit of the Reykjanes Ridge is at about 300-m depth at 63°N and deepens to more than 3,000 m at the CGFZ. Between 60°N and the CGFZ, the Reykjanes Ridge is cut by many fracture zones of increasing bottom depths toward the south, while summits constantly reach 1,100–1,300 m (Figure 2). Lying at the heart of the subpolar gyre and located on the pathways of the North Atlantic Current (NAC) and overflow waters toward the Irminger and Labrador Seas, the Reykjanes Ridge is a major obstacle for North Atlantic circulation (Figure 1) and a gateway to deep convection areas

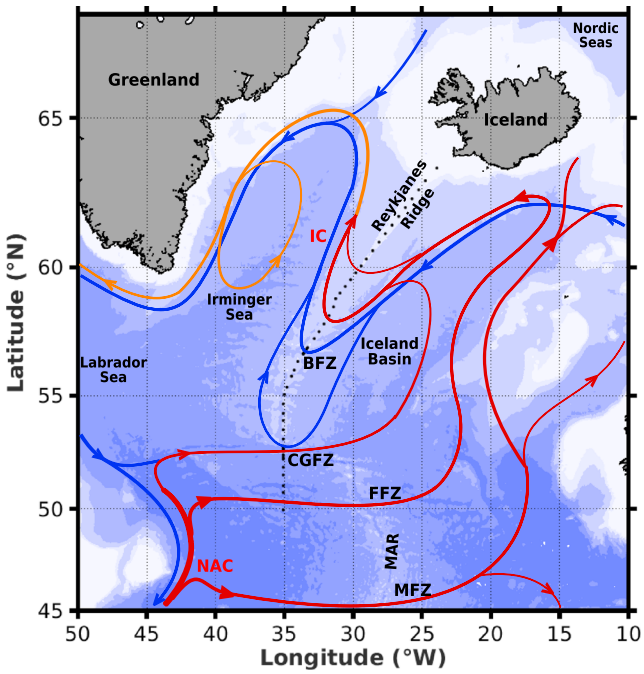

Figure 1. Schematic of large-scale circulation in the northern North Atlantic based on Daniault et al. (2016). Locations of the hydrographic stations where measurements were performed during the RREX15 cruise along the Reykjanes Ridge section are shown by black dots. Bathymetry is plotted in color with color changes at 500, 1,000, and every 1,000 m below 1,000 m. Topographical features and currents of the North Atlantic are indicated as follows: Bight Fracture Zone, Charlie-Gibbs Fracture Zone, Faraday Fracture Zone, Maxwell Fracture Zone, Mid-Atlantic Ridge, North Atlantic Current, and Irminger Current.

(Piron et al., 2017). Most likely, its seafloor roughness constrains deep circulation through mixing (de Lavergne et al., 2017).

The cyclonic circulation of the subpolar gyre extends roughly from 50 to 65°N (Figure 1). The eastward flowing NAC bounds the subpolar gyre to the south. At the MAR, three branches of the NAC are dynamically constrained by deep fracture zones: Maxwell Fracture Zone at 48°N, Faraday Fracture Zone (FFZ) at 50.5°N, and CGFZ at 52.5°N (Bower & Furey, 2017; Bower & von Appen, 2008; Roessler et al., 2015; Schott et al., 1999). The central NAC branch flowing near 50.5°N is characterized by a sharp salinity front and is generally referred to in the literature as the Sub-Arctic Front (SAF; Daniault et al., 2016). Above the Reykjanes Ridge, the westward flow of the subpolar gyre is fed by the NAC branches that flow cyclonically in the Iceland Basin and by deep flows from the Nordic Seas (Figure 1). RAFOS float trajectories showed that the westward branch of the subpolar gyre preferentially follows the BFZ at 57°N (Bower et al., 2002). Likewise, models showed that deep overflows from Iceland-Scotland Ridge preferentially join the Irminger Sea through the BFZ and CGFZ (Xu et al., 2010; Zou et al., 2017). Although the identification of those pathways through the fracture zones was a major step forward in our understanding of the subpolar gyre circulation, other analyses based on measurements perpendicular to the ridge axis suggested that the subpolar gyre takes additional pathways across the Reykjanes Ridge. For instance, the Ovide project provided series of indirect transport estimates showing significant westward transport north of the BFZ, although no specific fracture zones were identified there (Daniault et al., 2016; Lherminier et al., 2010). Chafik et al. (2014) and Childers et al. (2015) suggested that this westward transport is very weak between 0- and 400-m depth. The preferred pathways across the Reykjanes Ridge and the vertical structure of the flow thus remain unclear, as does the connection of the westward flows across the Reykjanes Ridge to the upstream NAC branches. Finally, most of the water masses crossing the Reykjanes Ridge westward (see section 2.5 for water mass description) undergo modifications in the Iceland Basin by air-sea exchange in the mixed layer, isopycnal and diapycnal mixing at intermediate depths, or entrainment in the deep overflows. Although the distribution and transport of these water masses by the subpolar gyre are known in the Iceland Basin, their distributions along the Reykjanes Ridge related to the circulation and the bathymetry have never been documented, and the associated transports have only been quantified in an integral way (Daniault et al., 2016; Garcia-Ibanez et al., 2015).

Until now, direct observations along the Reykjanes Ridge were lacking. As a result, no detailed view of volume and water mass transports was available for this area and subpolar gyre intensity had only been estimated on given densities (Bower et al., 2002), from proxies (Häkkinen & Rhines, 2004), or from general circulation models (Böning et al., 2006; Lohmann et al., 2009). A quantification of the water mass transports across the Reykjanes Ridge would provide benchmarks for the validation of ocean general circulation models, which are presently inadequate for representing the cross-ridge flows in the area (Penduff et al., 2007; Rattan et al., 2010).

This study aims to quantify the full water column transport above the Reykjanes Ridge, from Iceland to 50°N. It is based on a synoptic data set collected as part of the RREX project along the crest of the Reykjanes Ridge during June–July 2015. The effect of the bathymetry on the transport will be investigated by identifying the preferred pathways across the Reykjanes Ridge and by characterizing the vertical structure of the circulation.

This paper is organized as follows. Section 2 presents the data and method used for this study. The currents and associated transports across the Reykjanes Ridge are presented in section 3, including a

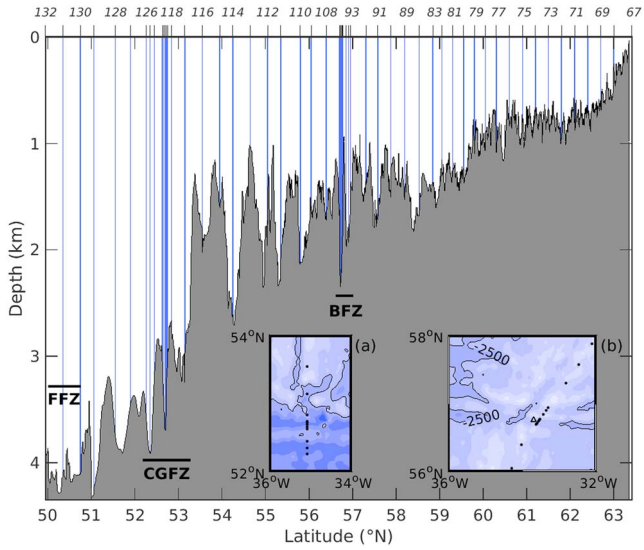

Figure 2. Locations of the hydrographic stations carried out along the top of the Reykjanes Ridge during the RREX15 cruise (blue vertical lines). The bathymetry (gray shading) was recorded by the ship echo sounder. Hydrographic station spacing was reduced in the Bight Fracture Zone (BFZ) and Charlie Gibbs Fracture Zone (CGFZ). The BFZ, CGFZ, and Faraday Fracture Zone are indicated. Inserted maps: (a) bathymetry in the CGFZ area with a 500-m isobath spacing. The black line outlines the −2,500-m isobath. Locations of stations 116 to 126 (black dots) are indicated; (b) bathymetry in the BFZ area with a 500-m isobath spacing. Locations of stations 92 to 101 and 107 to 109 (black dots) and of the main sill of the BFZ (black triangle) are indicated. The deepest bathymetries are represented with the darkest blue.

description of the water mass transports. In section 4, results are compared to previous findings and are discussed in a context of larger scale circulation and water mass transformation. Finally, results are summarized in section 5.

2. Data and Methods

2.1. Description of the Cruise

The RREX2015 cruise was carried out from 5 June to 10 July 2015 on the N/O Thalassa. $CTDO_2$ (conductivity temperature depth oxygen), nutrient, pH, and total alkalinity measurements were acquired at 56 stations along a section that extended from Iceland to 50°N (Figure 1). Referred to hereinafter as the Reykjanes Ridge section, this section was designed to study the exchanges of volume and properties between the Iceland Basin and the Irminger Sea above the Reykjanes Ridge and constitutes the main data source for this study. The Reykjanes Ridge section follows the crest of the Reykjanes Ridge from the Icelandic continental shelf to 53°N, while its southern part from 53°N to 50°N retraces Saunders (1994)'s hydrographic line along 35°W. Between 57.3 and 56.1°N, the section cuts the BFZ east of its main sill (Figure 2, inset). The nominal station spacing of 30 km was reduced to 2 km at the BFZ and CGFZ, at about 57°N and 52.5°N, respectively (Figure 2). The collection of measurements along the Reykjanes Ridge section was interrupted twice: a first time after station 83 to deploy moorings and a second time after station 101 to carry out hydrographic measurements west of the BFZ main sill. As a result, the time elapsed between station 83 and the following station along the section (station 88) was 34 hr. Similarly, the time elapsed between measurements at station 101 and the following station along the section (station 107) was 22 hr. Otherwise, the time between measurements at successive stations was less than 4 hr.

2.2. Data Sets

Temperature, conductivity, and dissolved oxygen were measured as a function of pressure at all hydrographic stations (Thierry et al., 2018), using a Seabird Electronics 911+ $CTDO_2$ probe mounted on a rosette equipped with 28 bottles. The rosette was stopped 15 m above the bottom. For $CTDO_2$ calibration purposes, seawater samples were analyzed on board for salinity and dissolved oxygen concentration. Temperature and pressure sensors were calibrated at the laboratory before and after the cruise, and no sensor drift was detected. The accuracies of the $CTDO_2$ measurements were found to be 1 dbar for pressure, 0.001 °C for temperature, 0.0025 for salinity, and 1 μmol kg^{-1} for dissolved oxygen (Branellec & Thierry, 2016). Figures 3 and 4 show vertical sections of hydrographic properties along the Reykjanes Ridge section and their distribution in the θ-S space.

The rosette was equipped with both upward and downward looking 300-kHz L-ADCPs (Lowered Acoustic Doppler Current Profiler, RD Instruments). The inverse method from Visbeck (2002) was used to process and combine these two data sets and to estimate the horizontal velocity profiles. The vertical cell size was set at 16 m, and the overall velocity error was estimated at 0.03 m s^{-1}. More details on the L-ADCP processing can be found in Lherminier et al. (2007).

Upper layer current velocity components were measured from the ship using two S-ADCPs (Shipboard Acoustic Doppler Current Profiler, RD Instruments) operating at 38 kHz (OS38) and 150 kHz (OS150; Thierry et al., 2018). In this study, we used the OS38 data only. The OS150 data were used to verify the OS38 calibration corrections (Petit et al., 2018). The bin size was set at 24 m, and the pinging rate was 3 s. The OS38 operated in narrowband mode, and the maximum depth reached was 1,300 m. Velocity profiles were averaged over 2-min ensembles by the acquisition software to decrease the

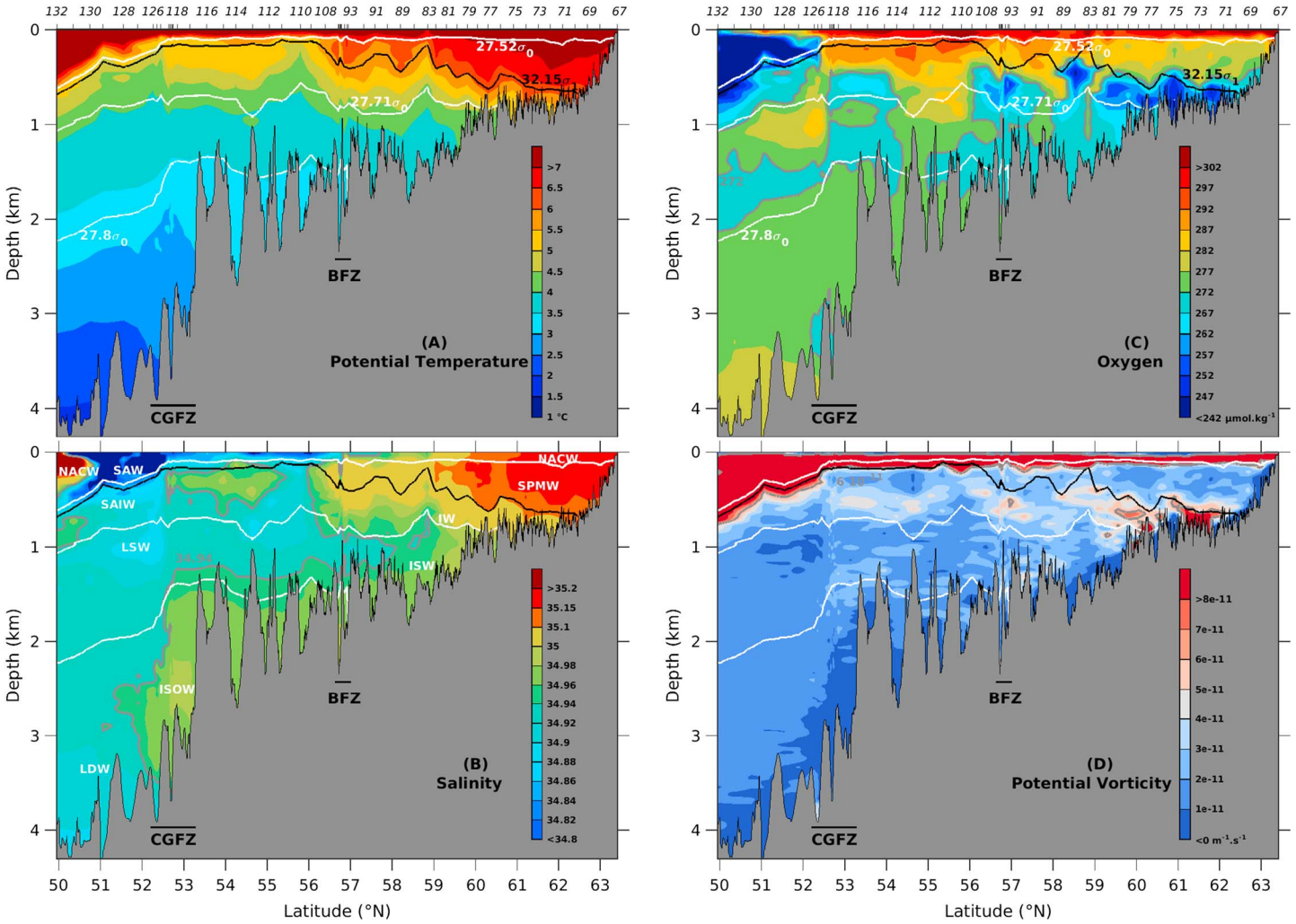

Figure 3. Hydrographic sections along the Reykjanes Ridge section based on CTDO$_2$ data: (a) potential temperature in °C; (b) salinity; (c) dissolved oxygen concentration in μmol kg^{-1}; (d) potential vorticity in m^{-1} s^{-1}. The bold black lines represent the potential density anomaly σ_1 = 32.15 kg m^{-3}. The bold gray lines show the isohaline 34.94 in (b), isoline 272 μmol kg^{-1} in (c), and isoline 6 · 10^{-11} m^{-1} s^{-1} in (d). In all panels, the bold white lines show the potential density anomalies σ_0 = 27.52, 27.71, and 27.8 kg m^{-3} that are used to delimit the identified water masses (see Table 1). Bathymetry in gray is from the ship survey. The BFZ and CGFZ are indicated.

measurement error. These ensembles were then processed using Cascade Version 7.0 ("Chaine Automatisée de Suivi des Courantomètres Acoustiques Doppler Embarqués"; Le Bot et al., 2011). Details of the processing are given in Petit et al. (2018). The mean departure of the ADCP from the horizontal was estimated at 0.3° by minimizing the vertical velocity. Misalignment and amplitude corrections were estimated at 0.05° and 1.0067 cm s^{-1}, respectively, using the bottom track procedure (Firing & Hummon, 2010). The barotropic tidal currents were removed from the 2-min averaged velocity data using TPXO8.0 OSU tidal prediction software based on the Tidal Data Inversion (Egbert & Erofeeva, 2002). Finally, S-ADCP data were averaged over 2-km segments along the Reykjanes Ridge section.

Bathymetry was measured every 30 s along the ship track using a 12-kHz echo sounder (Figure 2). The bathymetric model ETOPO1 (Amante & Eakins, 2009) was used to fill few gaps in the recorded bathymetry at around 52°N and 60.5°N.

Merged-Absolute Dynamic Topography from the Ssalto/Duacs AVISO (Archiving, Validation and Interpretation of Satellite Oceanographic data center) altimeter products distributed by Copernicus Marine

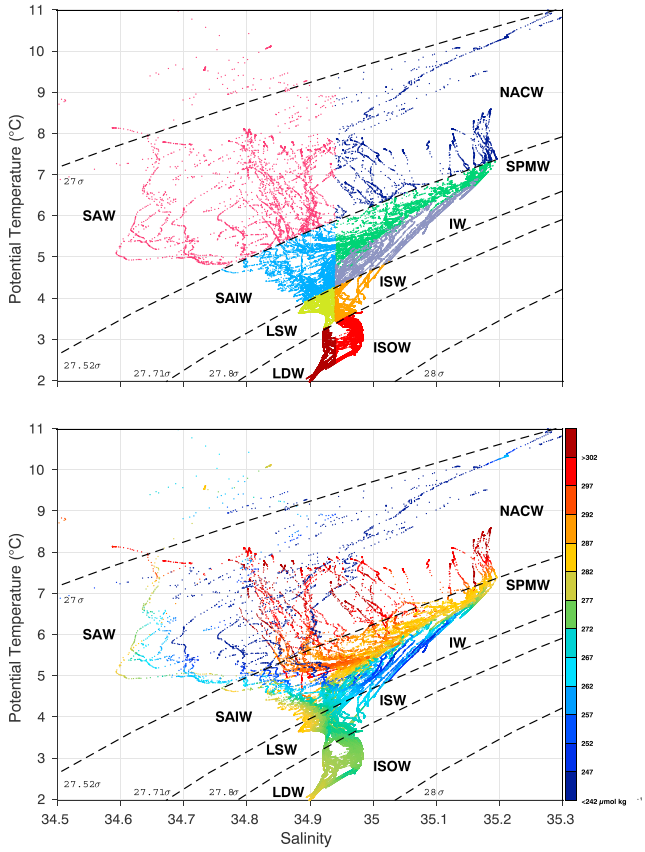

Figure 4. Potential temperature θ/*S* diagrams displaying all hydrographic profiles along the Reykjanes Ridge section. (top) Each water mass indicated in Table 1 is represented by a different color. (bottom) The colors correspond to oxygen concentration (μmol kg^{-1}). In the two panels, the dashed black lines indicate the isopycnals σ_0 = 27, 27.52, 27.71, 27.8, and 28 kg m^{-3}. The water masses indicated by their abbreviations are listed in Table 1.

Environment Monitoring Service on a 1/3° grid was used to compute time-averaged surface geostrophic velocities over the period from 5 June to 10 July 2015.

Wind stress data from the two global atmospheric reanalysis, ERA-Interim reanalysis (Dee et al., 2011) and National Centers for Environmental Prediction (NCEP)/National Center for Atmospheric Research reanalysis (Kalnay et al., 1996), were used to compute the Ekman transport at the location and time of measurements at each hydrographic station.

2.3. S-ADCP Referenced Geostrophic Velocities

Dynamic height referenced to the surface was computed from temperature, salinity, and pressure at all $CTDO_2$ stations. Their horizontal gradients were then computed between two adjacent stations and used in the thermal wind equation to compute geostrophic velocities referenced to the surface. In presence of a sloping topography, the geostrophic velocity between two $CTDO_2$ stations cannot be computed in the bottom triangle, which is to say below the deepest common level (DCL) of a pair of stations. To estimate the geostrophic flow in the bottom triangle, Ganachaud (2003) recommended the interpolation of hydrographic properties at the shallowest station from adjacent data. We used a second-order polynomial fit suggested by Ganachaud (2003) and computed hydrographic properties below the DCL at the shallowest station by second-order interpolation of the hydrographic properties at the DCL and below. Geostrophic velocities were computed in the bottom triangle of each pair of stations based on the interpolated dynamic heights. Because the interpolation led to unrealistic velocity at the station pair 114–115, the geostrophic velocity in the bottom triangle was computed as decreasing to zero at the bottom.

An absolute geostrophic field was estimated by adjusting the geostrophic field referenced to the surface to S-ADCP absolute velocity measurements following Lherminier et al. (2007) and Gourcuff et al. (2011). The absolute geostrophic profile was computed by adding a constant velocity correction to the geostrophic velocity profile referenced to the surface. The correction is the difference in a reference layer L_{ref} between the S-ADCP velocities horizontally averaged between the two stations of the pair and the geostrophic velocities referenced to the surface. To do this, it is best that the physical contents of the geostrophic and S-ADCP velocities in layer L_{ref} are as similar as possible. This means that we should avoid depths where ageostrophic motions, caused by bottom and wind frictions, interactions of tides with bathymetry, inertial oscillations, or cyclogeostrophic terms are the most intense (Ganachaud, 1999). Selecting L_{ref} = 600–1,000 m led to the best agreement between the geostrophic and S-ADCP profiles. In order to remove "small scale side effects" when averaging S-ADCP data over limited horizontal and vertical distances, we filtered the original 2-km × 16-m gridded S-ADCP velocities horizontally and vertically using Lanczos filters with respective cutoff wave numbers of 1/8 km^{-1} and 1/400 m^{-1} applied consecutively. The cutoff frequencies are of the order of magnitude of the Rossby radius horizontally and of L_{ref} thickness vertically. The filtering decreased significantly the root-mean-square (RMS) difference between the geostrophic velocities and the S-ADCP velocities. Above the BFZ and CGFZ, strong ageostrophic motions prevented robust determination of the reference velocity at the 2-km resolution allowed by the CTD sampling. A single reference velocity was thus estimated over the BFZ and CGFZ (stations 96–101 and 119–122, respectively). Figure 5 shows the resulting absolute geostrophic velocity section along the Reykjanes Ridge.

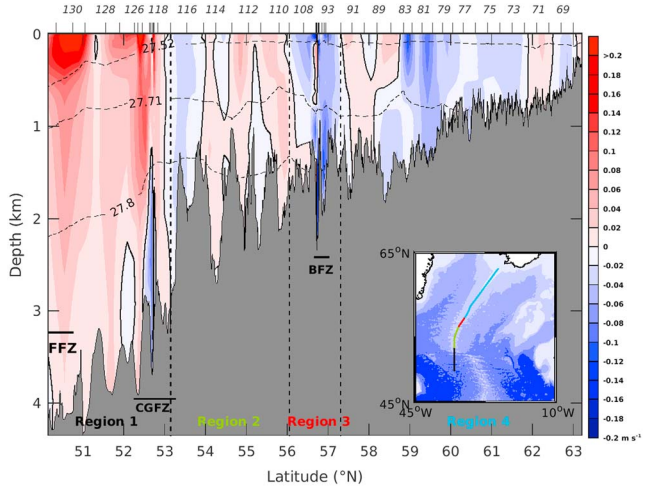

Figure 5. Velocity section along the Reykjanes Ridge section (m s^{-1}). Positive values correspond to eastward velocities. The dashed black lines indicate the potential density σ_0 = 27.52, 27.71 and 27.8 kg m^{-3}. Bathymetry is shown in gray. The dashed vertical black lines divide the section into four regions (see text). The locations of the hydrographic stations are indicated on the top axis. Insert: Map of the bathymetry of the North Atlantic with a 1,000-m spacing. The deepest bathymetries are represented with the darkest blue. The four regions along the Reykjanes Ridge section are shown with different colors.

2.4. Transport Estimates and Errors

Transport across the Reykjanes Ridge section is the sum of geostrophic and Ekman transports. To compute the geostrophic transport, each geostrophic velocity was assigned to a surface equal to the distance between the stations of each pair multiplied by the vertical resolution of the geostrophic velocity profile. Then, the transport for a region limited by the hydrographic stations in the horizontal, and constant depths, isopycnals, or bathymetry in the vertical, was computed as the sum of the products of the geostrophic velocities by the associated surfaces over the region considered. Figure 6 shows the resulting top-to-bottom integrated transport along the Reykjanes Ridge section cumulated from Iceland to 50°N.

Errors for the total transports were computed as follows. The main source of error in the geostrophic transports comes from errors in the determination of the reference velocity, which are the sum of errors due to S-ADCP instrumental noise $E_{\text{inst\_noise}}$, S-ADCP calibration error $E_{\text{inst\_bias}}$, and errors due to the presence of ageostrophic motions in the S-ADCP velocities E_{ageo}. An additional error E_{bott} comes from the extrapolation of the hydrographic properties in the bottom triangles (Ganachaud, 2003). The Ekman transport error E_{Ekman} mainly comes from the uncertainty in the wind stress data.

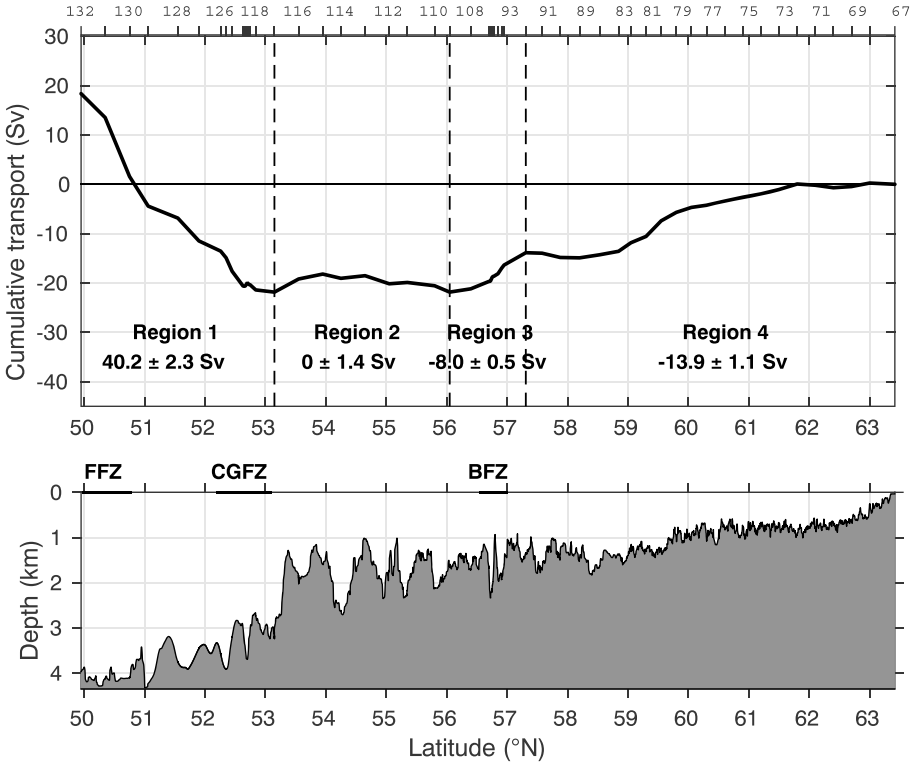

Figure 6. (top) Top-to-bottom vertically integrated transport (Sv) along the Reykjanes Ridge section cumulated from Iceland to 50°N. Increasing (decreasing) cumulative transport corresponds to eastward (westward) transport. The dashed lines divide the section into four regions (see text). The locations of the hydrographic stations are shown on the top axis. (bottom) Bathymetry along the Reykjanes Ridge section. CGFZ stands for Charlie Gibbs Fracture Zone, BFZ for Bight Fracture Zone, and FFZ for Faraday Fracture Zone.

Accounting for all contributions, the error in the total transports for a given region $E_{transport}$ can be written as

$$E_{transport} = \mathrm{sqrt}\left(\left[\delta_{layer}{}^{surface}\, E_{Ekman}{}^{2} + S.E_{ageo}{}^{2} + S.E_{inst\_noise}{}^{2} + \delta_{layer}{}^{bottom}\, E_{bott}{}^{2}\right]\right) + S.E_{inst\_bias} \quad (1)$$

where S is the surface of the area over which the transport is computed. $\delta_{layer}{}^{surface}$ and $\delta_{layer}{}^{bottom}$ are Kronecker deltas, indicating that those errors are taken into account only when the surface or bottom layers are included in the region. The errors are considered as random, except for the S-ADCP calibration error, which is a systematic error.

The instrumental error was estimated as the mono-ping standard deviation (0.23 m s^{-1}), given by the manufacturer, divided by the number of S-ADCP measurements used to calculate the referenced velocity. To obtain an error for the transport, E_{inst_noise} was multiplied by the surface S of the considered region. Over a horizontal distance of 30 km and a layer thickness of 1,500 m, E_{inst_noise} is equal to 0.01 Sv. Its contribution to the error on the top-to-bottom integrated transport along the Reykjanes Ridge section was estimated at 0.7 Sv.

To estimate the error for the absolute geostrophic velocity due to ageostrophic motions, we followed Lherminier et al. (2007) and considered the length scale Lg, set at half the Rossby radius, below which ageostrophic motions dominate. About half of the variance associated with these scales was removed by filtering the S-ADCP data as described above. We computed the variance of the S-ADCP signal in the layer L_{ref} for each Lg segment along the Reykjanes Ridge section. Then, assuming a decorrelation between ageostrophic signals for one Lg segment to the other, we computed an averaged ageostrophic variance for the region considered. At the first order, this variance is due to the sum of the ageostrophic signal and instrumental noise. We thus removed the instrument noise variance from the small-scale variance to obtain an estimate of the variance of the ageostrophic motions. This variance was then divided by N, with N the number of segments Lg in the horizontal for the area considered. The square root of this value, multiplied by the surface of the considered region, gives the ageostrophic transport error $S.E_{ageo}$. Typically, for a 30-km distance and a layer thickness of 1,500 m, the error was ~0.06 Sv. On the top-to-bottom integrated transport along the Reykjanes Ridge section, this error was estimated at 1 Sv.

The error E_{bott} due to the extrapolation of the hydrographic data in the bottom triangle was estimated by computing the RMS difference between the polynomial fit method used in this study with three other extrapolation methods proposed by Ganachaud (2003). The maximum value equal to 0.4 Sv was found at the station pair 124–125. The error, cumulated along the Reykjanes Ridge section, was estimated at 0.7 Sv.

The error in the Ekman transport (E_{Ekman}) was estimated as the RMS difference between ERA-Interim and NCEP Ekman transports. This error, cumulated along the Reykjanes Ridge section, was estimated at 0.04 Sv.

The instrumental bias E_{inst_bias} due to error in the S-ADCP misalignment correction was computed as the difference between the OS38 transport and OS150 transport (both corrected for misalignment) in the part of the water column where the signals overlapped. The bias was estimated at $8 \cdot 10^{-4}$ m s^{-1}, which corresponds to a 2.7-Sv bias for the top-to-bottom transport once cumulated along the Reykjanes Ridge section.

Finally, because it took 10 days to carry out the measurements along the Reykjanes Ridge section, the data are not fully synoptic. To evaluate this asynopticity, we computed the RMS difference in AVISO surface velocities between the beginning (24 June 2015) and the end (5 July 2015) of the section. This RMS difference is equal to 0.015 m s^{-1}, which is marginally significant given the 0.03-m s^{-1} error for AVISO velocities (Gourcuff et al., 2011). Although this asynopticity error may be underestimated because of the smoothing used for generating AVISO products, this result suggests that the asynopticity error is negligible.

2.5. Water Mass Characterization

By referring to the literature and to properties observed along the Reykjanes Ridge section (Figures 3 and 4), we identified four layers delimited by isopycnals that encompass nine main water masses. Layer 1, defined by

Table 1
Criteria Based on Limits and Ranges of Potential Density (σ_0), Salinity (S), Dissolved Oxygen Concentration (O_2), and Potential Vorticity (q) for the Identification of the Water Masses Along the Reykjanes Ridge Section

Water masses	Potential density (kg m^{-3})	Salinity	Oxygen (μmol kg^{-1})	Potential vorticity (m^{-1} s^{-1})
NACW	$\sigma_0 < 27.52$	$S > 34.94$		
SAW	$\sigma_0 < 27.52$	$S < 34.94$		
SAIW	$27.52 < \sigma_0 < 27.71$	$S < 34.94$		
IW	$27.52 < \sigma_0 < 27.71$	$S > 34.94$	$O_2 < 272$	
SPMW	$27.52 < \sigma_0 < 27.71$	$S > 34.94$	$O_2 > 272$	$q < 6 \cdot 10^{-11}$
LSW	$27.71 < \sigma_0 < 27.8$	$S < 34.94$		
ISW	$27.71 < \sigma_0 < 27.8$	$S > 34.94$		
LDW	$\sigma_0 > 27.8$	$S < 34.94$		
ISOW	$\sigma_0 > 27.8$	$S > 34.94$		

Note. These limits and ranges are shown in Figure 3. NACW stands for North Atlantic Central Water, SAW for Sub-Arctic Water, SAIW for Sub-Arctic Intermediate Water, IW for Intermediate Water, SPMW for Subpolar Mode Water, LSW for Labrador Sea Water, ISW for Icelandic Slope Water, LDW for Lower Deep Water, and ISOW for Iceland-Scotland Overflow Water.

$\sigma_0 < 27.52$ kg m^{-3}, contains North Atlantic Central Water (NACW) of subtropical origin (Iselin, 1936) and Sub-Arctic Water (SAW) of subpolar origin (Dickson et al., 1988). These water masses are separated by a sharp salinity front defined by approximately 34.94 at station 130 and separating NACW to the south from SAW to the north. Further north, a weaker salinity front near station 91 separates SAW to the south from NACW to the north. There, NACW properties differ from those observed south of station 130 due to air-sea heat loss in the Iceland Basin (Figure 4).

Layer 2, defined by $27.52 < \sigma_0 < 27.71$ kg m^{-3}, contains Sub-Arctic Intermediate Water (SAIW) of subpolar origin and is characterized by salinity below 34.94 (Arhan, 1990) and Subpolar Mode Water (SPMW) with salinity above 34.94 and relatively low potential vorticity ($q < 6.10^{-11}$ m^{-1} s^{-1}). The potential vorticity was computed as $q = \frac{-f}{\rho_0}\frac{\partial \rho}{\partial z}$, where f is the Coriolis parameter, ρ_0 is the reference density, and ρ is the potential density referenced to the middepth interval over which the vertical gradient of density is computed. The homogeneous SPMW is formed in the winter mixed layer and may also be fed by underlying intermediate waters when the winter mixed layer is deep enough (Brambilla & Talley, 2008; de Boisséson et al., 2012; Thierry et al., 2008). Layer 2 also contains Intermediate Water (IW) associated with patches of low oxygen concentration ($O_2 < 272$ μmol kg^{-1}) and high salinity ($S > 34.94$) and lies just above the isopycnal 27.71 in the northern part of the Reykjanes Ridge and in the NAC. Carried by the Gulf Stream and subsequently by the NAC, the aged IW is biogeochemically defined by minima of O_2 and maxima of NO_3 (Van Aken & De Boer, 1995).

Layer 3, defined by $27.71 < \sigma_0 < 27.8$ kg m^{-3}, encompasses Labrador Sea Water (LSW) that is formed by deep convection in the Irminger and Labrador Seas and has a relative minimum in salinity ($S < 34.94$; Sy et al., 1997; Van Aken et al., 2011). The layer also contains Icelandic Slope Water (ISW) of higher salinity and lower dissolved oxygen concentration than LSW. ISW is formed close to the Iceland-Faroe Ridge by mixing between SPMW and overflow waters and is further transformed by isopycnal mixing with LSW while flowing southward along the Reykjanes Ridge (Read, 2001).

Finally, Layer 4, defined by $\sigma_0 > 27.8$ kg m^{-3}, contains Iceland-Scotland Overflow Water (ISOW), which flows along the eastern flank of the Reykjanes Ridge from the Iceland-Scotland Ridge and is characterized by salinity above 34.94 (Kanzow & Zenk, 2014; Saunders, 1994). Transported by the subtropical branch of the NAC, layer 4 also encompasses Lower Deep Water (LDW) characterized by salinity below 34.94, potential temperature below 3 °C, and a relative high concentration of dissolved oxygen ($O_2 > 278$ μmol kg^{-1}) and dissolved silicic acid ($Si(OH)_4 > 18$ μmol kg^{-1}, not shown). LDW is formed by mixing of diluted overflow waters from the north and diluted Antarctic Bottom Water from the south (McCartney, 1992).

Criteria for the identification of each water mass based on the above description are given in Table 1 (see also Figure 4). These criteria will be used below to determine the spatial distribution of each water mass along the Reykjanes Ridge section and the associated transports. The transport for a given station pair was computed by integrating the velocity field over the surface occupied by the water mass at this station pair.

3. Results: Transports Across the Reykjanes Ridge

3.1. The Top-to-Bottom Cross-Ridge Flow

We computed the top-to-bottom vertically integrated transports, cumulated southward from Iceland (Figure 6), from the absolute geostrophic velocities (Figure 5). Positive values correspond to eastward velocities. Starting from Iceland, the cumulative transport decreases until 56.1°N, indicating a westward flow. This flow is intensified between 62 and 59°N and above the BFZ, between 57.3 and 56.1°N, revealing two main cross-ridge flows. Between 56.1 and 53.15°N, the cumulative transport reaches a plateau, indicating weak flows of opposite direction. South of 53.15°N, the transport sharply increases corresponding to an eastward flow.

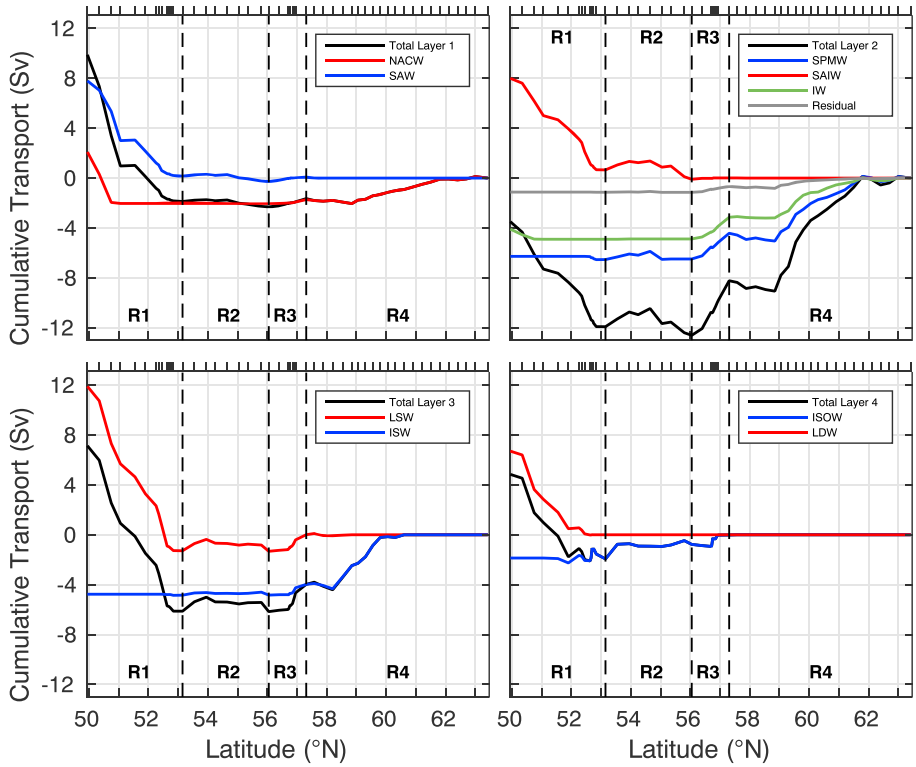

Figure 7. Transports (Sv) across the Reykjanes Ridge section (black lines) cumulated from Iceland to 50°N and integrated into layer 1 in the upper-left panel, layer 2 in the upper-right panel, layer 3 in the lower-left panel, and layer 4 in the lower-right panel. The blue lines indicate the transports for SAW (upper-left panel), SPMW (upper-right panel), ISW (lower-left panel), and ISOW (lower-right panel). The red lines indicate the transports for NACW (upper-left panel), SAIW (upper-right panel), LSW (lower-left panel), and LDW (lower-right panel). The green line indicates the transports for IW, and the gray line indicates the residual transport (upper-right panel). These transports are integrated as defined in Table 1. Locations of the hydrographic stations are given at the top of the upper panels (black ticks).

A first quantification of the cross-ridge transports was obtained by considering the cumulative transports in four regions (Figure 6). Region 1 (south of 53.15°N) not only delimits the eastward flowing NAC but also encompasses some of the westward flow of ISOW at the CGFZ. In region 1, the top-to-bottom integrated transport was estimated at 40.2 ± 2.3 Sv. As revealed by the absolute geostrophic velocity section (Figure 5), the NAC divides in two branches that are respectively aligned with the FFZ, centered at 50.5°N, and the CGFZ, centered at 52.5°N. The top-to-bottom transports of the two NAC branches over the FFZ and CGFZ were estimated at 22.8 ± 1.1 and 17.4 ± 1.7 Sv, respectively. From the northern boundary of region 1 to the Icelandic slope, relatively intense westward flows alternate with relatively weak eastward flows (Figure 5). Region 2 (between 53.15 and 56.1°N) is located south of the BFZ and is characterized by no net flow (0 ± 1.4 Sv, Figure 6). The top-to-bottom transports in the two main pathways at the BFZ (region 3 between 56.1 and 57.3°N) and at 59–62°N were estimated at −8.0 ± 0.5 and −13.6 ± 0.8 Sv, respectively. The overall transport in regions 2–4, which corresponds to the intensity of the subpolar gyre, was estimated at −21.9 ± 2.5 Sv.

3.2. Water Mass Transports Across the Reykjanes Ridge

To quantify the contributions of the water masses to the cross-ridge flow, we computed their transport according to the water mass definition (Table 1) in the density layers they belong to. We then cumulated these transports from Iceland to 50°N (Figure 7) and in the four regions (Figure 8).

Layer 1 thickness varies strongly with latitude, from ~600 m at 50°N to ~200 m north of 53°N (Figure 3). Accordingly, the bulk of the transport in this layer occurs to the south of the section in the NAC (region 1).

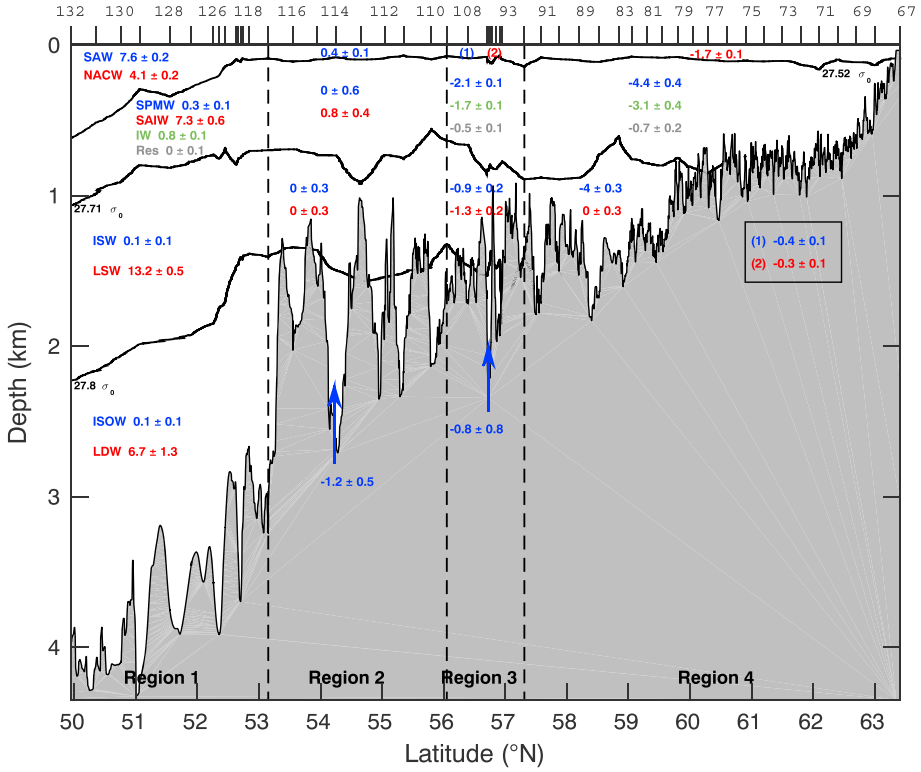

Figure 8. Transports (Sv) of each water mass (as identified in Table 1) integrated over each box encompassed by the isopycnals σ_0 = 27.52, 27.71, and 27.8 kg m^{-3} (solid black lines) and by the four regions (dashed black lines). The colors in regions 2 to 4 relate to the water mass acronyms shown in region 1.

Here the eastward transports of SAW and NACW were estimated at 8.0 ± 0.2 Sv and 4.1 ± 0.2 Sv, respectively (Figures 7 and 8). No NACW was transported in region 2, but a westward flow of NACW was also observed in regions 3 and 4 (−2.0 ± 0.1 Sv).

In layer 2 (Figures 7 and 8), SAIW was transported eastward by the NAC in region 1 (7.3 ± 0.6 Sv). A weak eastward flow of IW was also observed in the southern part of region 1 (0.8 ± 0.1 Sv). The residual transport (−1.2 ± 0.2 Sv) is associated with a stratified (potential vorticity $> 6 \cdot 10^{-11}$ m^{-1} s^{-1}) water mass, observed in the upper part of this layer, with the same salinity and oxygen characteristics as SPMW ($S > 34.94$ and $O_2 > 272$ μmol kg^{-1}). In regions 2–4, the SPMW transport was estimated at −6.5 ± 0.9 Sv and intensified at the BFZ (−2.1 ± 0.1 Sv) and 59–62°N (−5.2 ± 0.4 Sv). Similarly, the IW transport was estimated at −4.8 ± 0.4 Sv in regions 2–4 and intensified at the BFZ (−1.7 ± 0.1 Sv) and 59–62°N (−3.2 ± 0.4 Sv).

In layer 3, LSW of relatively high oxygen concentration ($O_2 > 272$ μmol kg^{-1} in Figure 3) flows eastward in region 1 and between 54 and 56.1°N in region 2 with transports of 13.2 ± 0.5 Sv and 0.9 ± 0.6 Sv, respectively (Figure 7). In between these eastward flows as well as at the BFZ, relative low oxygen concentration and high salinity indicate modified LSW flowing westward with a transport of −0.9 ± 0.1 Sv between 53.15 and 54°N in region 2 and −1.3 ± 0.2 Sv at the BFZ. The cross-ridge flow of ISW (−4.8 ± 0.5 Sv) occurs mainly between 58.3°N and 60°N in region 4. Further north, the Reykjanes Ridge is not deep enough to allow the crossing of ISW that lies deeper than 800 m.

In layer 4, no deep waters cross the Reykjanes Ridge section north of the BFZ (Figures 7 and 8). LDW flows eastward south of and through the southern valley of the CGFZ (south of 52.5°N). The net LDW transport was estimated at 6.7 ± 1.3 Sv. ISOW crosses the Reykjanes Ridge at the BFZ and CGFZ (stations 116–126) with transports of −0.8 ± 0.8 Sv and −1.1 ± 0.7 Sv, respectively, while a net ISOW transport of 0 ± 0.4 Sv was estimated between the BFZ and CGFZ.

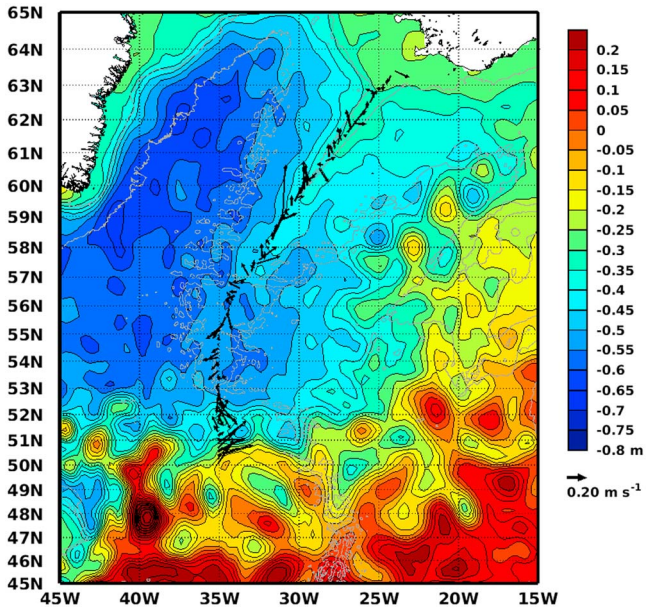

Figure 9. Absolute dynamic topography (m) of the subpolar gyre averaged between 24 June and 5 July 2015. The black vectors indicate the surface velocities (m s^{-1}) along the Reykjanes Ridge section during the cruise. Bathymetries of −1,500 and −2,500 m are outlined in gray.

4. Discussion

In this section, we first discuss the circulation observed across the Reykjanes Ridge in the wider context of the subpolar circulation based on an AVISO altimetry map (Figure 9). We then discuss the distribution and evolution of all the water masses along the Reykjanes Ridge, focusing in more detail on SPMW and IW, and then on ISOW. Finally, by comparing the inflow with the outflow across the section, we discuss the water mass transformation occurring in the Iceland Basin.

4.1. Circulation Across the Reykjanes Ridge

The AVISO altimetry map (Figure 9) provides a view of circulation in the Subpolar North Atlantic at the time of the cruise. It shows complex structures at the ocean surface with multiple eddies and meanders associated with the NAC as well as the cyclonic circulation in the Iceland Basin and the anticyclonic circulation around the Reykjanes Ridge fed by the NAC. The AVISO altimetry map reveals that, at the time of the cruise, the NAC was composed of three different branches at 46–47°N, 50–51°N, and 52–53°N. The latter two branches were sampled by our data set north of 50°N (Figure 5). These are the northern NAC branch and the SAF reported in Daniault et al. (2016), the latter being associated with a sharp salinity front. The top-to-bottom integrated transport of the NAC was estimated at 40.2 ± 2.3 Sv in region 1. Although this synoptic estimate is high compared to the 2002–2012 mean transport (24.2 ± 5 Sv) reported by Daniault et al. (2016), it lies within the observed range of variability (see Figure 2 in Daniault et al., 2016). During the cruise, the strong intensity of the NAC could be due either to eddies or meanders, as shown by Roessler et al. (2015) and Bower and von Appen (2008), or to time variability at a longer time scale. Indeed, Roessler et al. (2015) and Breckenfelder et al. (2017) demonstrated a link between the intensity of the NAC and the NAO, with a more vigorous NAC during a positive NAO state, which was the case in 2015 (Piron et al., 2017).

The westward flow of the subpolar gyre occurs in two main branches: at the BFZ and at 59–62°N (Figure 5). The BFZ pathway is consistent with Bower et al. (2002) who showed, based on an analysis of acoustically tracked floats drifting at σ_0 = 27.5 and 27.7 kg m^{-3}, that cross-ridge flows occur preferentially over fracture zones. The westward pathway at the BFZ is also seen at 1,000 dbar on the mean current map derived from Argo float trajectories (see Figure 7 in Ollitrault & Colin de Verdière, 2014). Our data set provides the first direct estimate of the cross-ridge flow magnitude in the surroundings of the BFZ (−8.0 ± 0.5 Sv) and shows that its minimum is at middepth, with similar amplitudes at the ocean surface and ocean bottom (Figure 5).

The presence of a westward pathway in the northern part of the Reykjanes Ridge (north of the BFZ) has been subject to controversy in the literature. Using S-ADCP sections averaged over 1999–2002, Chafik et al. (2014) found almost no transport in the upper 400 m of the water column above the Reykjanes Ridge between Iceland and 59.5°N. In contrast, using an inverse box model, Lherminier et al. (2010) estimated westward top-to-bottom cross-ridge transports of 9.6 ± 2.1 Sv in 2002 and 13.8 ± 2.1 Sv in 2004 between Iceland and 58.5°N. Using an extended data set spanning 2002–2010, Garcia-Ibanez et al. (2015) computed a westward mean transport of 9.4 ± 4.7 Sv at the same location. Our top-to-bottom integrated westward transport of 14.3 ± 0.8 Sv between Iceland and 58.5°N is consistent with the latter results, showing a significant cross-ridge flow north of 58.5°N.

As pointed out by Daniault et al. (2016), the difference between the results of Chafik et al. (2014) and those of Lherminier et al. (2010) and Garcia-Ibanez et al. (2015) could be related to the difference in latitude between their data sets as well as to the difference in the vertical range used for the transport computations. We used our data set to check these hypotheses. The transport of the upper 400 m was estimated at −6.5 ± 0.5 Sv between Iceland and 58.5°N and at −3.9 ± 0.4 Sv between Iceland and

59.5°N, which is much lower than our top-to-bottom transport estimates. These results show some dependence on the southern latitude limit used for the transport computations and confirm that the major factor was the limited layer (0–400 m) used by Chafik et al. (2014). Additional differences from Chafik et al. (2014) might be caused by time variability and the spread of the locations of the S-ADCP sections averaged by Chafik et al. (2014), which spanned a large latitudinal band around the 59–62°N pathway (Figure 5). This makes the interpretation of Chafik et al. (2014)'s results somehow difficult, given the sensitivity of transport estimates to the choice of the southern latitude limit. Interestingly, the westward pathway north of 58.5°N is also followed by the Argo floats at 1,000 dbar, suggesting that this could be a permanent feature (see Figure 7 in Ollitrault & Colin de Verdière, 2014). The bathymetry shows a sharp deepening between 60 and 58.3°N, which might be the reason for the location of the intensified westward flow there (Figure 6). Indeed, 67% of the top-to-bottom transport in region 4 occurs between 60 and 58.3°N.

4.2. NAC Water Masses

In region 1, which encompasses the entire northern branch and most of the middle branch of the NAC, the NAC water masses are of subtropical origin (NACW, IW, and LDW) and subpolar origin (SAW, SAIW, LSW, and ISOW; Figures 7 and 8). Recalling that the NAC is both the eastward limb of the subpolar gyre carrying subpolar waters and the upper limb of the Meridional Overturning Circulation (MOC) carrying subtropical waters, the respective intensities of subtropical and subpolar origin waters in the NAC give us some insight into the relative strengths of each circulation branch. We estimated these intensities as the ratio of subpolar or subtropical water transports divided by the overall eastward flow (40.2 ± 2.3 Sv). In total, the NAC transported a larger proportion of subpolar waters (71.1%). Indeed, the three main water masses contributing to the NAC, LSW (32.8%), SAW (18.9%), and SAIW (18.2%), are of subpolar origin. The proportion of subpolar waters was greater in the northern branch (83.6%) than in the SAF (61.4%). The larger influence of subpolar water masses compared to subtropical ones reflects a stronger contribution of the subpolar gyre than the MOC to these branches.

4.3. Subpolar Mode Water and Intermediate Water

Subpolar Mode Water and IW were seen to be major components of the westward branch of the subpolar gyre, representing 29.7% and 21.9% of the westward transport in regions 2–4, respectively.

In two areas along the Reykjanes Ridge, SPMW shows nearly homogeneous densities around σ_0 = 27.56 kg m^{-3} from 59 to 63°N and σ_0 = 27.61 kg m^{-3} from 53 to 55.5°N (Figure 10). The transition between these two pools occurs at the BFZ. SPMW salinity and potential temperature vary progressively from 35.17–7.1 °C at 63°N to 34.95–5.2 °C at 53°N, but the temperature/salinity variations are density-compensated in each pool. In a similar way to our results, de Boisséson (2010, see Figure 2.10 therein) found a southward increase in SPMW density over the Reykjanes Ridge that he attributed to the circulation and water mass composition of the NAC branches in the Iceland Basin. The model showed that SPMW transported by the westward flow north of 59°N was fed by the SAF, while that transported by the flow at the BFZ was fed by the northern branch of the NAC. As the northern branch carries colder water masses than the SAF (Figure 3), SPMW found at the BFZ was denser than that observed further north. In our data, the connection of the SAF with the westward flow at 59–62°N is supported by the distribution of the NACW along the Reykjanes Ridge section. This water mass, which was only present in the SAF (south of 51°N), was observed north of 59°N but not above the BFZ. This is further confirmed by the AVISO sea surface height map shown in Figure 9. Isolines suggest that, after looping in the Iceland Basin, the northern branch of the NAC and the SAF are connected to the westward flows at the BFZ and 59–62°N, respectively.

Although the cumulated transport of SPMW is low in region 2 (Figure 8), the patch of SPMW seen at 53–55.5°N is associated with an eastward transport (Figure 7). This patch of dense (σ_0 = 27.61 kg m^{-3}, Figure 10) SPMW does not seem to be related to a branch of the NAC. It suggests a different formation mechanism from that discussed by de Boisséson et al. (2012). In Brambilla and Talley (2008), the dense variety of SPMW found at 53–55.5°N belongs to a tongue of SPMW extending eastward to the Irminger Sea at the center of the cyclonic gyre, as indicated by the temperature distribution on the 27.5σ_0 isopycnal (see Figures 4 and 7 in Brambilla & Talley, 2008). This cyclonic circulation associated with weaker stratification

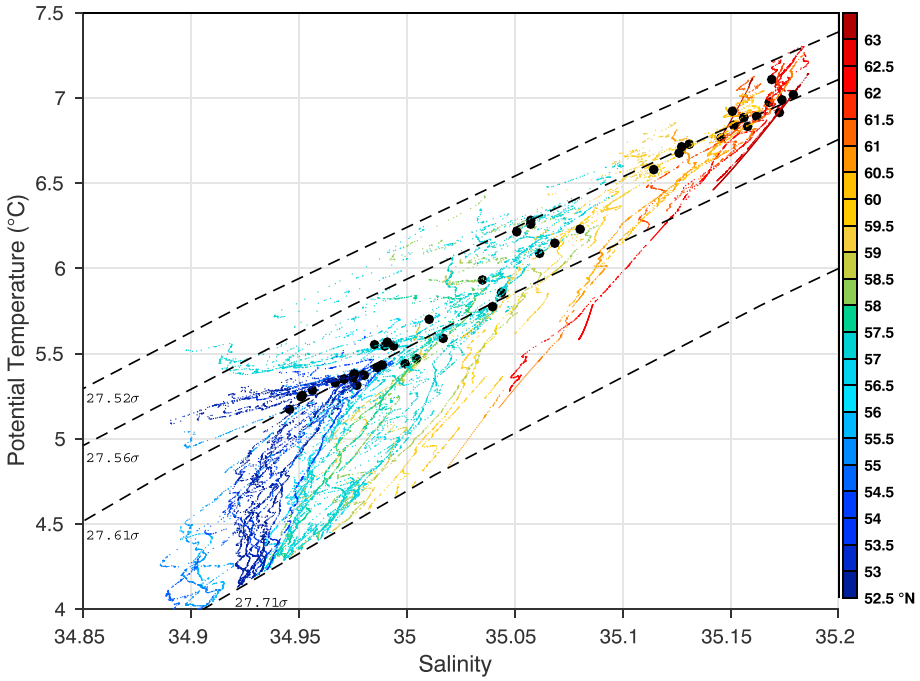

Figure 10. Potential temperature θ/*S* diagram displaying all hydrographic profiles of Subpolar Mode Water (SPMW) as defined in Table 1. The locations of the profiles along the Reykjanes Ridge section (°N) are shown in color. For all profiles, the black dots mark the hydrologic properties at the minimum of potential vorticity in the SPMW layer. The dashed black lines indicate the isopycnals σ_0 = 27.52, 27.56, 27.61, and 27.71 kg m^{-3}.

at its center, also shown by Bower et al. (2002), could favor localized formation of dense SPMW close to its center.

Intermediate Water, characterized by the lowest oxygen, was found in the SAF with an eastward transport of 0.8 ± 0.1 Sv and at the BFZ and 59–62°N with westward transports of 3.2 ± 0.4 and 1.7 ± 0.1 Sv, respectively (Figures 3, 7, and 8). The NAC northern branch contains only SAIW in the layer 2. In the SAF, the IW properties (34.94–4.5 °C) are similar to those of Antarctic Intermediate Water observed by Harvey and Arhan (1988, see Figure 11 therein). IW observed at 59–62°N is characterized by salinity and temperature of 35.1 and 6.5 °C, respectively. The fresher and colder IW at the BFZ (34.9–4.8 °C) could be more influenced by SAIW.

4.4. Iceland-Scotland Overflow Water

In the CGFZ, the westward flow of ISOW through the northern valley is almost entirely compensated by an eastward flow of ISOW through the southern valley (Figure 7). Analyzing high-resolution ocean circulation models, Xu et al. (2010) found an ISOW flow over the Reykjanes Ridge occurring through the BFZ and CGFZ, but also north of the BFZ. This latter pathway, which is not observed in our data set, could be related to the fact that ISOW density was lower in the model than in the observations. Despite these limitations, Xu et al. (2010) and Zou et al. (2017) estimated a mean transport of −1.2 ± 0.1 Sv north of the CGFZ, consistent with our observations.

Our estimate of ISOW transport through the CGFZ during the cruise is weaker than that found in past studies. Xu et al. (2010) and Saunders (1994) found an ISOW transport of −2.4 ± 0.5 Sv through the CGFZ. More recently, Bower and Furey (2017) studied the evolution of ISOW transport through the CGFZ using an array of eight moorings deployed between 2010 and 2012. They estimated an ISOW time-averaged transport of −1.7 ± 0.5 Sv but showed that the ISOW flow varied strongly between intense westward events and weaker westward or even eastward events. The low-frequency variability of ISOW transport through the CGFZ is mainly correlated with the variability of the deep-reaching branches of the NAC. During eastward events, the northern branch of the NAC is localized over the northern valley and the westward ISOW flow is limited to the northern wall of the CGFZ.

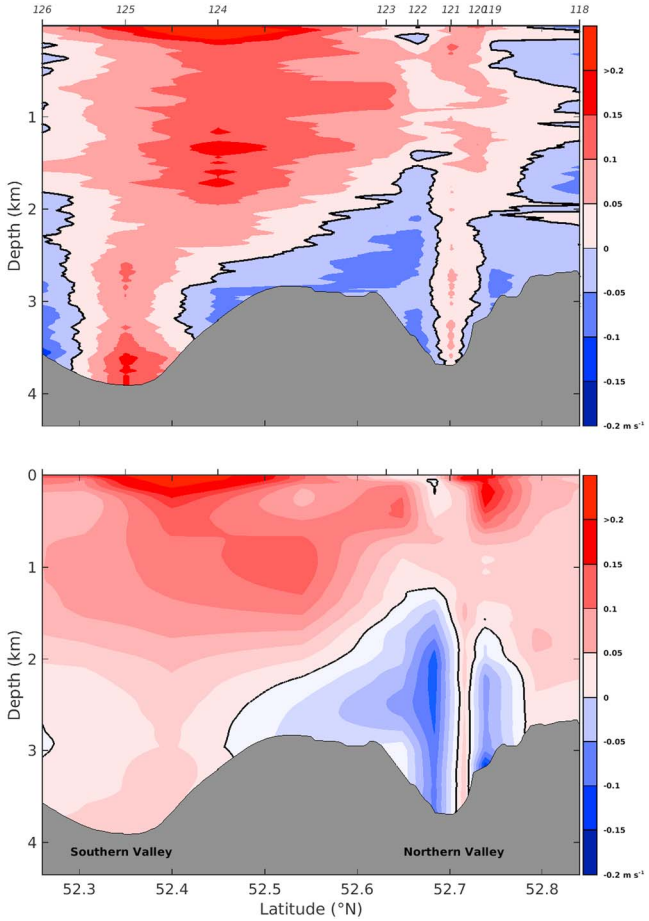

Figure 11. (top) Lowered Acoustic Doppler Current Profiler and (bottom) geostrophic velocity sections in the Charlie Gibbs Fracture Zone (m s^{-1}). Positive values correspond to eastward velocities. The bathymetry from the ship is shown in gray with the locations of the two valleys. The locations of the hydrographic stations are given on the top axis.

In Figure 11, we show the profiles of geostrophic and L-ADCP velocities in the CGFZ (52.35°N–52.9°N). L-ADCP measurements provide local velocities at each station, while geostrophic velocities are average velocities between stations (Lherminier et al., 2007), so we cannot expect a perfect agreement between the two data sets. Nevertheless, the dynamical structures were in good agreement in the strong eastward currents associated with the northern branch of the NAC that occupied the northern and southern valleys of the CGFZ from the surface down to the bottom. In the northern valley, the flow of ISOW was split in two at 52.72°N by a top-to-bottom eastward vein of the NAC or a deep reaching eddy.

Based on Bower and Furey (2017), the velocity profiles recorded in the period 3–5 July 2015 were not typical of extreme eastward events, characterized by maximum NAC surface velocities located over the northern valley. The deep-reaching branch of the NAC was instead localized above the southern valley with a surface speed of 0.23 m s^{-1}. Bower and von Appen (2008) specified that a minimum surface speed of 0.15 m s^{-1} is required to disturb the ISOW flow. During the RREX2015 cruise, the NAC was thus to the north and strong enough to disturb the flow of ISOW, but not sufficiently far north to block or reverse it in the CGFZ.

4.5. Water Mass Transformations

We will now consider the contributions of the water masses to the MOC. We base our discussion on Figure 12, which shows the transports integrated by region and plotted as a function of density appropriately showing the water mass transformations. Note that our interpretation of Figure 12 is made in terms of water mass transformations along pathways connecting the northern NAC branch and the SAF to the westward flow over the Reykjanes Ridge and mixing of the Iceland-Scotland overflows. Following Mercier et al. (2015), we consider the water masses that are less dense (denser) than σ_1 = 32.15 kg m^{-3} (or σ_0 = 27.6 kg m^{-3}) to belong to the upper (lower) limb of the MOC (Figure 3). In region 1, the MOC upper limb is composed of NACW, SAW, and some SAIW (Figure 12), which flow eastward toward the Iceland Basin at a rate of 12.9 ± 0.2 Sv. In regions 2–4, the MOC upper limb is mainly composed of weakly stratified SPMW in regions 3 and 4, and NACW in region 4, with hardly any contribution of SAW or SAIW. These water masses flow westward at a rate of 8.8 ± 0.6 Sv. The NACW transport in the westward flow is maximal at σ_0 = 27.38 kg m^{-3} (region 4, Figure 12), while it occurs at lower density in the SAF (σ_0 = 27–27.25 kg m^{-3}, Figure 4). SPMW shows maximum transport at σ_0 = 27.56 kg m^{-3} in region 4 and weaker transport at σ_0 = 27.6 kg m^{-3} in the BFZ (region 3). The stratified NACW and SAW transported by the NAC are thus transformed into denser and less stratified SPMW by air-sea buoyancy loss (de Boisséson et al., 2012). This densification mostly occurs within the upper limb of the MOC and paves the way for further densification occurring downstream in the Irminger Sea and feeding of the lower limb of the MOC (Sarafanov et al., 2012).

In the MOC lower limb ($\sigma_1 > 32.15$ kg m^{-3}), the maximum transport in the NAC is associated with an eastward transport of LSW at σ_0 = 27.72 kg m^{-3}, while weaker westward transport of LSW is found at σ_0 = 27.73 kg m^{-3} in the BFZ and at 27.75 kg m^{-3} in region 4 (Figure 12). In regions 2–4, both ISW (−4.9 ± 0.3 Sv) and IW (−4.8 ± 0.4 Sv) contribute more to the westward transport across the Reykjanes Ridge than does the sum of LSW (−1.3 ± 0.7 Sv) and ISOW (−2.0 ± 0.9 Sv; Figure 8). The maximum transport of ISW around σ_0 = 27.78 kg m^{-3} in region 4 reveals the modal characteristic of this water mass. ISW is not only formed by local entrainment and mixing of SPMW and ISOW but also incorporates LSW by isopycnal mixing, which partly explains the small cross-ridge transport associated with LSW in our diagnostic.

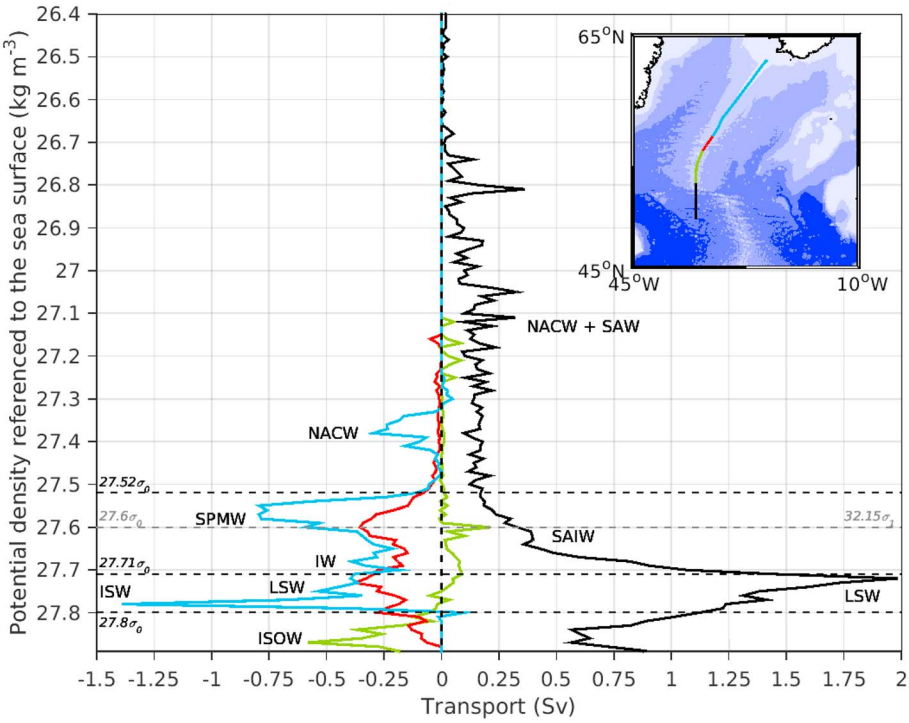

Figure 12. Transport integrated in 0.01 bins of density σ_0 for the four regions identified in Figure 6: Region 1 is shown in black (50–53.15°N), region 2 in green (53.15–56.1°N), region 3 in red (56.1–57.3°N), and region 4 in blue (57.3°N, Iceland). The horizontal dashed black lines indicate the potential density σ_0 = 27.52, 27.71 and 27.8 kg m^{-3}. The dashed gray line indicates the potential density σ_1 = 32.15 kg m^{-3}. Some water masses listed in Table 1 are associated with a peak of maximum transport.

5. Conclusions

During June–July 2015, the circulation and hydrography was recorded by 2 S-ADCPs and at 56 CTDO$_2$ stations along the crest of the Reykjanes Ridge, from the Icelandic continental shelf south to 50°N. The associated geostrophic transports were estimated by combining S-ADCP and hydrographic data. These observations provide the first direct estimates of exchanges of volume and properties between the Iceland Basin and the Irminger Sea across the Reykjanes Ridge.

Before entering the Iceland Basin, the NAC crosses the MAR following deep fracture zones. During June–July 2015, the NAC was in a northern position, such that we identified two surface-intensified branches north of 50°N that followed the CGFZ and FFZ. These branches correspond to the northern branch of the NAC and to the SAF as identified in the literature (Daniault et al., 2016) and were associated with top-to-bottom transports of 17.4 ± 1.7 and 22.8 ± 1.1 Sv, respectively. Compared to the portion of the SAF measured in this study, which contains 61.4% of subpolar waters and 38.6% of subtropical waters, the northern branch contains a larger proportion of subpolar waters, representing 83.6% of its top-to-bottom transport. In the surface layers, the NAC transported highly stratified water masses, while at deeper levels it transported LSW at a density of σ_0 = 27.72 kg m^{-3}. This latter water mass was the main contributor to the NAC and represented 32.8% of its top-to-bottom integrated transport.

The westward flow across the Reykjanes Ridge was estimated at −21.9 ± 2.5 Sv and represents the first direct estimate of subpolar gyre intensity. This flow follows two main passages: at 59–62°N with a transport of −13.6 ± 0.8 Sv and through the BFZ with a transport of −8.0 ± 0.5 Sv. As these pathways are already present in other data sets, they are likely permanent features related to the bottom topography. The flows at the BFZ (Bower & von Appen, 2008) and at about 60°N were associated with a sharp deepening of the crest of the Reykjanes Ridge. In terms of water masses, the three main contributors to the top-to-bottom westward flow were SPMW (29.7%), ISW (22.3%), and IW (21.9%), while the contributions of ISOW and LSW were only 9.1% and 5.9%, respectively. SPMW found at and south of the BFZ (σ_0 = 27.61 kg m^{-3}) was denser than SPMW

found at 59–62°N (σ_0 = 27.56 kg m^{-3}) as a result of cyclonic circulation in the Iceland Basin connecting the SAF to 59–62°N and the northern NAC branch to the BFZ. At greater depths, IW and ISW also crossed the Reykjanes Ridge following these two pathways. However, the westward flow of ISW was strictly localized south of 60°N because the Reykjanes Ridge is not deep enough to allow the transport of ISW north of this latitude.

Iceland-Scotland Overflow Water crossed the Reykjanes Ridge between 52°N and 57.3°N; no sign of ISOW was recorded north of the BFZ. Through the BFZ and south of it, ISOW transports were estimated at −0.8 ± 0.8 and −1.1 ± 0.7 Sv, respectively. These results compare favorably with those from numerical models (Xu et al., 2010; Zou et al., 2017), although the ISOW transport through the CGFZ was weak, as a consequence of the position and strength of the northern branch of the NAC in summer 2015 that disturbed the ISOW flow in the CGFZ (Bower & Furey, 2017).

Finally, our data set shows that large water mass transformations and densifications occurred in the Iceland Basin. Densification did not lead to a significant light-to-dense conversion of the water masses from the upper to the lower limb of the MOC, but it preconditioned the water column by forming weakly stratified water masses, especially SPMW, that favor the downstream overturning occurring in the Irminger Sea.

Acknowledgments

The authors thank all colleagues and ship crews involved in the hydrographic acquisition of the RREX 2015 cruise data discussed in this paper. T. Petit and V. Thierry were supported by the French Institute for the Exploitation of the Sea (IFREMER, Plouzané, France), and H. Mercier by the French National Center for Scientific Research (CNRS). T. Petit was also co-funded by the Brittany Region (France). The RREX project is funded by IFREMER, INSU/LEFE (Institut National des Sciences de l'Univers/Les enveloppes fluides et l'Environnement), Brittany Region, CG29 (Conseil Général du Finistère, France), and BMO (Brest Metropole Ocean, France). The work was supported by the French Oceanographic Fleet (TGIR FOF) for the realization of the RREX15 cruise on board the French R/V *Thalassa*. This is a contribution to the AtlantOS project funded by the European Union's Horizon 2020 research and innovation program under grant agreement 633211. Data are available in the repository doi: 10.17882/55445 (Thierry et al., 2018). The AVISO altimeter data were downloaded from the Copernicus Marine Environment Monitoring Service website (http://marine.copernicus.eu/services-portfolio/access-to-products/). The ERA-Interim reanalysis data were downloaded from the ECMWF (European Center for Medium-range Weather Forecasts) website (http://apps.ecmwf.int/datasets/). The NCEP/National Center for Atmospheric Research reanalysis data were downloaded from the NOAA (National Oceanic and Atmospheric Administration) website (https://www.esrl.noaa.gov/psd/data/gridded/data.ncep.reanalysis.html).

References

Amante, C., & Eakins, B. W. (2009). ETOPO1 1 arc-minute global relief model: Procedures, data sources and analysis, National Geophysical Data Center, NOAA. Retrieved from https://www.ngdc.noaa.gov/mgg/global/relief/ETOPO1/docs/ETOPO1.pdf

Arhan, M. (1990). The North Atlantic Current and Subarctic Intermediate Water. *Journal of Marine Research*, *48*(1), 109–144. https://doi.org/10.1357/002224090784984605

Böning, C. W., Scheinert, M., Dengg, J., Biastoch, A., & Funk, A. (2006). Decadal variability of subpolar gyre transport and its reverberation in the North Atlantic overturning. *Geophysical Research Letters*, *33*, L21S01. https://doi.org/10.1029/2006GL026906

Bower, A., & Furey, H. (2017). Iceland-Scotland overflow water transport variability through the Charlie-Gibbs fracture zone and the impact of the North Atlantic Current. *Journal of Geophysical Research: Oceans*, *122*, 6989–7012. https://doi.org/10.1002/2017JC012698

Bower, A. S., Le Cann, B., Rossby, T., Zenk, W., Gould, J., Speer, K., et al. (2002). Directly measured mid-depth circulation in the northeastern North Atlantic Ocean. *Nature*, *419*(6907), 603–607. https://doi.org/10.1038/nature01078

Bower, A. S., & von Appen, W.-J. (2008). Interannual variability in the pathways of the North Atlantic Current over the Mid-Atlantic Ridge and the impact of topography. *Journal of Physical Oceanography*, *38*(1), 104–120. https://doi.org/10.1175/2007JPO3686.1

Brambilla, E., & Talley, L. D. (2008). Subpolar Mode Water in the northeastern Atlantic: 1. Averaged properties and mean circulation. *Journal of Geophysical Research*, *113*, C04025. https://doi.org/10.1029/2006JC004062

Branellec, P., & Thierry, V. (2016). RREX 2015. CTD-O2 data report. ODE/LOPS/16–26. http://doi.org/10.13155/47156

Breckenfelder, T., Rhein, M., Roessler, A., Boning, C. W., Biastoch, A., Behrens, E., & Mertens, C. (2017). Flow paths and variability of the North Atlantic Current: A comparison of observations and a high-resolution model. *Journal of Geophysical Research: Oceans*, *122*, 2686–2708. https://doi.org/10.1002/2016JC012444

Chafik, L., Rossby, T., & Schrum, C. (2014). On the spatial structure and temporal variability of poleward transport between Scotland and Greenland. *Journal of Geophysical Research: Oceans*, *119*, 824–841. https://doi.org/10.1002/2013JC009287

Childers, K. H., Flagg, C. N., Rossby, T., & Schrum, C. (2015). Directly measured currents and estimated transport pathways of Atlantic Water between 59.5°N and the Iceland-Faroes-Scotland Ridge. *Tellus A*, *67*, 28067. https://doi.org/10.3402/tellusa.v67.28067

Daniault, N., Mercier, H., Lherminier, P., Sarafanov, A., Falina, A., Zunino, P., et al. (2016). The northern North Atlantic Ocean mean circulation in the early 21st century. *Journal of Progress in Oceanography*, *146*, 142–158. https://doi.org/10.1016/j.pocean.2016.06.007

de Boisséson, E. (2010). Eaux modales subpolaires du Bassin d'Islande: Origine, formation et variabilité, PhD Thesis of University of Bretagne Occidentale, Brest, France.

de Boisséson, E., Thierry, V., Mercier, H., Caniaux, G., & Desbruyeres, D. (2012). Origin, formation and variability of the Subpolar Mode Water located over the Reykjanes Ridge. *Journal of Geophysical Research*, *117*, C12005. https://doi.org/10.1029/2011JC007519

de Lavergne, C., Madec, G., Holmes, R. M., & McDougall, T. J. (2017). Abyssal Ocean overturning shaped by seafloor distribution. *Nature*, *551*(7679), 181–186. https://doi.org/10.1038/nature24472

Dee, D. P., Uppala, S. M., & Simmons, A. J. (2011). The ERA-Interim reanalysis: Configuration and performance of the data assimilation system. *Quarterly Journal of the Royal Meteorological Society*, *137*(656), 553–597. https://doi.org/10.1002/qj.828

Dickson, R., Meincke, J., Malmberg, S., & Lee, A. J. (1988). The great salinity anomaly in the northern North Atlantic. *Progress in Oceanography*, *20*(2), 103–151. https://doi.org/10.1016/0079-6611(88)90049-3

Egbert, G. D., & Erofeeva, S. Y. (2002). Efficient inverse modeling of Barotropic Ocean tides. *Journal of Atmospheric and Oceanic Technology*, *19*(2), 183–204. https://doi.org/10.1175/1520-0426(2002)019<0183:EIMOBO>2.0.CO;2

Firing, E., & Hummon, J. M. (2010). Shipboard adcp measurements, the GO-SHIP repeat hydrography manual: A collection of expert reports and guidelines, IOCCP Report 14. Retrieved from https://www.go-ship.org/Manual/Firing_SADCP.pdf

Ganachaud, A. (1999). Large scale oceanic circulation and fluxes of freshwater, heat, nutrients and oxygen, PhD Thesis of Massachusetts Institute of technology-Woods Hole Oceanographic Institution.

Ganachaud, A. (2003). Error budget of inverse box models: The North Atlantic. *Journal of Atmospheric and Oceanic Technology*, *20*(11), 1641–1655. https://doi.org/10.1175/1520-0426(2003)020<1641:EBOIBM>2.0.CO;2

Garcia-Ibanez, M., Pardo, P., Carracedo, L., Mercier, H., Lherminier, P., Rios, A., & Perez, F. (2015). Structure, transports and transformations of the water masses in the Atlantic subpolar gyre. *Progress in Oceanography*, *135*, 18–36. https://doi.org/10.1016/j.pocean.2015.03.009

Gourcuff, C., Lherminier, P., Mercier, H., Traon, L., & Yves, P. (2011). Altimetry combined with hydrography for ocean transport estimation. *Journal of Atmospheric and Oceanic Technology*, *28*(10), 1324–1337. https://doi.org/10.1175/2011JTECHO818.1

Häkkinen, S., & Rhines, P. (2004). Decline of subpolar North Atlantic circulation during the 1990s. *Science*, *304*(5670), 555–559. https://doi.org/10.1126/science.1094917

Harvey, J., & Arhan, M. (1988). The water masses of the Central North Atlantic in 1983–1984. *Journal of Physical Oceanography*, *18*(12), 1855–1875. https://doi.org/10.1175/1520-0485(1988)018<1855:TWMOTC>2.0.CO;2

Iselin, C. (1936). The influence of the Mediterranean outflow at mid-depths in the Sargasso Sea, transactions. *American Geophysical Union*, *17*(1), 219. https://doi.org/10.1029/TR017i001p00219

Kalnay, E., Kanamitsu, M., Kistler, R., Collins, W., Deaven, D., Gandin, L., et al. (1996). The NCEP/NCAR 40-year reanalysis project. *Bulletin of the American Meteorological Society*, *77*(3), 437–471. https://doi.org/10.1175/1520-0477(1996)077<0437:TNYRP>2.0.CO;2

Kanzow, T., & Zenk, W. (2014). Structure and transport of the Iceland Scotland Overflow plume along the Reykjanes Ridge in the Iceland Basin. *Deep-Sea Research Part I: Oceanographic Research Papers*, *86*, 82–93. https://doi.org/10.1016/j.dsr.2013.11.003

Le Bot, P., Kermabon, C., Lherminier, P., & Gaillard, F. (2011). CASCADE V6.1: Logiciel de validation et de visualisation des mesures ADCP de coque, OPS/LPO 11-01. Retrieved from http://archimer.ifremer.fr/doc/00342/45285/

Lherminier, P., Mercier, H., Gourcuff, C., Alvarez, M., Bacon, S., & Kermabon, C. (2007). Transports across the 2002 Greenland-Portugal Ovide section and comparison with 1997. *Journal of Geophysical Research*, *112*, C07003. https://doi.org/10.1029/2006JC003716

Lherminier, P., Mercier, H., Huck, T., Gourcuff, C., Perez, F. F., Morin, P., et al. (2010). The Atlantic Meridional Overturning Circulation and the subpolar gyre observed at the A25-OVIDE section in June 2002 and 2004. *Deep Sea Research Part I: Oceanographic Research Papers*, *57*(11), 1374–1391. https://doi.org/10.1016/j.dsr.2010.07.009

Lohmann, K., Drange, H., & Bentsen, M. (2009). A possible mechanism for the strong weakening of the North Atlantic subpolar gyre in the mid-1990s. *Geophysical Research Letters*, *36*, L15602. https://doi.org/10.1029/2009GL039166

McCartney, M. S. (1992). Recirculating components to the deep boundary current of the northern North Atlantic. *Progress in Oceanography*, *29*(4), 283–383. https://doi.org/10.1016/0079-6611(92)90006-L

Mercier, H., Lherminier, P., Sarafanov, A., Gaillard, F., Daniault, N., Desbruyères, D., et al. (2015). Variability of the meridional overturning circulation at the Greenland-Portugal OVIDE section from 1993 to 2010. *Progress in Oceanography*, *132*, 250–261. https://doi.org/10.1016/j.pocean.2013.11.001

Ollitrault, M., & Colin de Verdière, A. (2014). The ocean general circulation near 1000-m depth. *Journal of Physical Oceanography*, *44*(1), 384–409. https://doi.org/10.1175/JPO-D-13-030.1

Penduff, T., Le Sommer, J., Barnier, B., Treguier, A. M., Molines, J. M., & Madec, G. (2007). Influence of numerical schemes on current-topography interactions in ¼ degrees global ocean simulations. *Ocean Science*, *3*(4), 509–524. https://doi.org/10.5194/os-3-509-2007

Petit, T., Thierry, V., & Mercier, H. (2018). RREX 2015: S-ADCP data processing report, LOPS/18–01 (March 2018). http://doi.org/10.13155/53471

Piron, A., Thierry, V., Mercier, H., & Caniaux, G. (2017). Gyre-scale deep convection in the subpolar North Atlantic Ocean during winter 2014–2015. *Geophysical Research Letters*, *44*, 1439–1447. https://doi.org/10.1002/2016GL071895

Rattan, S., Myers, P. G., Treguier, A. M., Theetten, S., Biastoch, A., & Boning, C. (2010). Towards an understanding of Labrador Sea salinity drift in eddy-permitting simulations. *Elsevier SCI LTD*, *35*(1-2), 77–88. https://doi.org/10.1016/j.ocemod.2010.06.007

Read, J. F. (2001). CONVEX-91: Water masses and circulation of the Northeast Atlantic subpolar gyre. *Progress in Oceanography*, *48*(4), 461–510. https://doi.org/10.1016/S0079-6611(01)00011-8

Roessler, A., Rhein, M., Kieke, D., & Mertens, C. (2015). Long-term observations of North Atlantic Current transport at the gateway between western and eastern Atlantic. *Journal of Geophysical Research: Oceans*, *120*, 4003–4027. https://doi.org/10.1002/2014JC010662

Sarafanov, A., Falina, A., Mercier, H., Sokov, A., Lherminier, P., Gourcuff, C., et al. (2012). Mean full-depth summer circulation and transports at the northern periphery of the Atlantic Ocean in the 2000s. *Journal of Geophysical Research*, *117*, C01014. https://doi.org/10.1029/2011JC007572

Saunders, P. M. (1994). The flux of overflow water through the Charlie-Gibbs fracture zone. *Journal of Geophysical Research*, *99*(C6), 12,343–12,355. https://doi.org/10.1029/94JC00527

Schott, F., Stramma, L., & Fischer, J. (1999). Interaction of the North Atlantic Current with the deep Charlie Gibbs Fracture Zone throughflow. *Geophysical Research Letters*, *26*(3), 369–372. https://doi.org/10.1029/1998GL900223

Sy, A., Rheint, M., Lazier, J. R. N., Koltermann, K. P., Meincke, J., Putzka, A., & Bersch, M. (1997). Surprisingly rapid spreading of newly formed intermediate waters across the North Atlantic Ocean. *Nature*, *386*, 675–679. https://doi.org/10.1038/386675a0

Thierry, V., de Boisséson, E., & Mercier, H. (2008). Interannual variability of the Subpolar Mode Water properties over the Reykjanes Ridge during 1990-2006. *Journal of Geophysical Research*, *113*, C04016. https://doi.org/10.1029/2007JC004443

Thierry, V., Mercier, H., Petit, T., Branellec, P., & Balem, K. (2018). Reykjanes Ridge experiment (RREX) dataset. *SEANOE*. http://doi.org/10.17882/55445

Van Aken, H., Femke de Jong, M., & Yashayaev, I. (2011). Decadal and multi-decadal variability of Labrador Sea water in the North-Western North Atlantic Ocean derived from tracer distributions: Heat budget, ventilation, and advection. *Deep Sea Research Part I: Oceanographic Research Papers*, *58*(5), 505–523. https://doi.org/10.1016/j.dsr.2011.02.008

Van Aken, H. M., & De Boer, C. J. (1995). On the synoptic hydrography of intermediate and deep water masses in the Iceland Basin. *Deep Sea Research Part I: Oceanographic Research Papers*, *42*(2), 165–189. https://doi.org/10.1016/0967-0637(94)00042-Q

Visbeck, M. (2002). Deep velocity profiling using acoustic Doppler current profilers: Bottom track and inverse solutions. *Journal of Atmospheric and Oceanic Technology*, *19*(5), 794–807. https://doi.org/10.1175/1520-0426(2002)019<0794:DVPULA>2.0.CO;2

Xu, X., Schmitz, W. J., Hurlburt, H. E., Hogan, P. J., & Chassignet, E. P. (2010). Transport of Nordic seas overflow water into and within the Irminger Sea: An eddy-resolving simulation and observations. *Journal of Geophysical Research*, *115*, C12048. https://doi.org/10.1029/2010JC006351

Zou, S., Lozier, S., Zenk, W., Bower, A., & Johns, W. (2017). Observed and modeled pathways of the Iceland Scotland overflow water in the eastern North Atlantic. *Progress in Oceanography*, *159*, 211–222. https://doi.org/10.1016/j.pocean.2017.10.003